Vortex spin-torque oscillator using $Co_2Fe_xMn_{1-x}Si$ Heusler alloys

Tatsuya Yamamoto,[1,*] Takeshi Seki,[1,2,3] and Koki Takanashi[1,3]
[1]*Institute for Materials Research, Tohoku University, Sendai 980-8577, Japan*
[2]*PRESTO, Japan Science and Technology Agency, Saitama 322-0012, Japan*
[3]*Center for Spintronics Research Network, Tohoku University, Sendai 980-8577, Japan*
(Received 1 July 2016; revised manuscript received 23 August 2016; published 16 September 2016)

We show spin-transfer-torque-driven vortex oscillations in current-perpendicular-to-plane giant magnetoresistance junctions using epitaxially grown $Co_2Fe_xMn_{1-x}Si$ (CFMS) Heusler alloy thin films. The soft magnetic property and high spin polarization of CFMS enable us to realize vortex oscillation emitting large microwave power with a low threshold current. The output power is maximized for a certain Fe-Mn composition ratio associated with a reduction of the threshold current for the oscillation, which is in agreement with a general model for spin-torque oscillation. Through comparison with an analytical theory that describes the translational motion of a vortex core, we show that the vortex core motion excited in the present device is inhomogeneous along the thickness direction. In spite of the inhomogeneity, the gyration radius at the CFMS/spacer interface region was estimated to be ~75% of the actual ferromagnetic layer radius, which indicates that the CFMS-based all-metallic junction is useful for achieving large-amplitude vortex core motion. This comprehensive investigation would also be useful for designing high-performance all-metallic nano-oscillators based on magnetic vortex dynamics.

DOI: 10.1103/PhysRevB.94.094419

I. INTRODUCTION

A spin-polarized current exerts torque on magnetization as it passes through a ferromagnet, which is called spin-transfer torque (STT) [1,2]. STT enables us to switch the magnetization direction by applying an electric current [3–5]. Moreover, under a certain condition, self-sustained magnetization precession can be excited by applying a dc current [6–9]. A spin-torque oscillator (STO) is a nanoscaled oscillator that converts magnetization dynamics to a microwave power through magnetoresistance effects, e.g., giant magnetoresistance (GMR) [7,10], tunneling magnetoresistance (TMR) [11,12], and anisotropic magnetoresistance (AMR) [13].

Among various types of STOs, vortex STOs [14,15], where the magnetizations in ferromagnetic layer(s) form a vortex structure, exhibit the narrowest oscillation linewidth (Δf) as well as the highest oscillation quality factor ($f_0/\Delta f$, f_0: oscillation frequency) at present. The stability of vortex oscillation originates from the topologically stable magnetic structure and good consistency of the magnetization distribution with the spatial distribution of the Oersted field formed by the dc current. Because of these features, vortex STOs are useful for simplifying the physical mechanism of spin-torque oscillation and can serve as model non-isochronous auto-oscillators [16]. Vortex STOs also provide a playground for investigating various intriguing phenomena including antivortices-mediated synchronization [17], and commensurability and chaos in vortex dynamics [18].

In addition to the studies on fundamental physical phenomena, recently, there have been several reports demonstrating a large output power (P_{out}) exceeding 10 nW through the application of MgO-based magnetic tunneling junctions (MTJs) to vortex STOs [19,20], which open up potential applications of vortex STOs. In contrast to the MTJ-based vortex STO, an output power P_{out} larger than 1 nW has not yet been achieved for the all-metallic vortex GMR-STO even though GMR-STOs are still advantageous compared with MTJ-STOs from the fact that they are capable of operating in a wide range of electric currents. This feature is especially beneficial for the vortex STO since the Oersted field formed by the dc current plays an important role in the stability of the magnetic vortex and the frequency tunability [14,21]. Also, unlike MTJ-STOs, GMR-STOs are free from dielectric breakdown, which leads to superior device reliability. In spite of the above benefits from the scientific and practical points of view, studies on vortex GMR-STOs are limited because of their low P_{out} typically of the order of pW [14,15].

To realize a large P_{out} in GMR-STOs, it is necessary to enhance the GMR of the junction. One candidate solution is utilizing highly spin-polarized Heusler alloys. Some ferromagnetic Heusler alloys are known to sustain their high spin polarizations even at room temperature, and their high spin-polarization gives rise to large GMR effects [22–30]. We have developed GMR-STOs using Co-based Heusler alloys and demonstrated that utilizing highly spin-polarized Heusler alloys is promising to enhance the output power P_{out} of GMR-STOs [31–33]. In addition to the high spin polarization, Co_2(Fe,Mn)Si (CFMS) Heusler alloys are blessed with low magnetization damping constants [34] and magnetic softness, i.e., a small magnetocrystalline anisotropy and small coercivity [35,36]. The low magnetization damping constants would be useful for reducing the threshold current for spin-torque oscillation (I_{th}) while the magnetic softness is suitable for controlling the magnetization configuration by means of microfabrication. Indeed, we recently demonstrated the formation of magnetic vortices in epitaxially grown CFMS circular disks [37], which in turn led to our interest in applying CFMS for the vortex GMR-STO.

In this study, we show STT-driven vortex oscillation in microfabricated devices using CFMS with varying Fe concentrations (x) in $Co_2Fe_xMn_{1-x}Si$. The series of devices with different x enables us to systematically investigate the

*tyamamoto@imr.tohoku.ac.jp

composition dependencies of the magnetic properties and the oscillation characteristics for CFMS. A clear relationship is observed between P_{out} and I_{th} for spin-torque oscillation. An enhancement of P_{out} and a reduction of I_{th} are achieved simultaneously at a certain x, which can be understood in the general framework of a spin-torque oscillator. Also, we quantitatively estimate the radius of the trajectory of vortex core gyration. The estimated radii indicate the achievement of large-amplitude vortex core motion.

II. EXPERIMENTAL METHODS

Thin films with a stacking structure of Cr (20)/Ag (20)/CFMS (20)/Ag (5)/CFMS (30)/Ag (2)/Au (3) (thickness in nm) were prepared on single-crystalline MgO (001) substrates by using an ultrahigh vacuum compatible magnetron sputtering system with a base pressure below 10^{-7} Pa. The Cr buffer layer was deposited at room temperature and was subsequently *in situ* annealed at 600 °C to achieve a flat surface. The Ag buffer layer and the CFMS/Ag/CFMS GMR stack were then deposited at room temperature and were again *in situ* annealed at 500 °C to promote chemical ordering. Here, the Fe-Mn composition ratios of the CFMS layers were controlled by co-sputtering Co_2MnSi and Co_2FeSi alloy targets. After annealing, the sample was cooled down to room temperature, and the Ag/Au capping layer was deposited on the top CFMS layer. The growth mode and the crystal structure of the prepared CFMS films were investigated by reflection high energy electron diffraction (RHEED) and x-ray diffraction (XRD) with Cu–Kα radiation. The $B2$ and $L2_1$ order parameters (S_{B2} and S_{L2_1}) of the prepared films were evaluated by using the following equations [38]:

$$S_{B2} = \sqrt{\frac{I_{200}^{\mathrm{obs}}}{I_{400}^{\mathrm{obs}}} \bigg/ \frac{I_{200}^{\mathrm{cal}}}{I_{400}^{\mathrm{cal}}}}, \tag{1}$$

$$S_{L2_1} = \frac{2}{3 - S_{B2}} \sqrt{\frac{I_{111}^{\mathrm{obs}}}{I_{220}^{\mathrm{obs}}} \bigg/ \frac{I_{111}^{\mathrm{cal}}}{I_{220}^{\mathrm{cal}}}}, \tag{2}$$

where I^{obs} (I^{cal}) is the experimentally observed (calculated) integrated value of peak intensity of the corresponding XRD peaks.

The magnetic properties of unpatterned films were investigated by using a vibrating sample magnetometer (VSM). Thin films were cut into $\sim 4 \times 4$ mm^2 pieces, and magnetization curves were measured by applying an in-plane magnetic field (H) along either the CFMS [100] or the CFMS [110] directions, which correspond to the MgO [110] and MgO [100] directions, respectively.

Devices were fabricated by employing electron-beam lithography, photolithography, and Ar-ion beam etching. The device structure is schematically illustrated in Fig. 1(a) along with an rf circuit used for microwave measurement. The top CFMS layer with a thickness (L) of 30 nm was patterned into a circular disk with a nominal diameter ($2r_0$) of 240 nm to stabilize a magnetic vortex at the remanent state [37], while the 20-nm-thick bottom CFMS layer remained unpatterned to serve as a reference layer for the spin-torque oscillation. Figure 1(b) shows a scanning electron microscopy image of a microfabricated nanopillar. After the etching process, the size

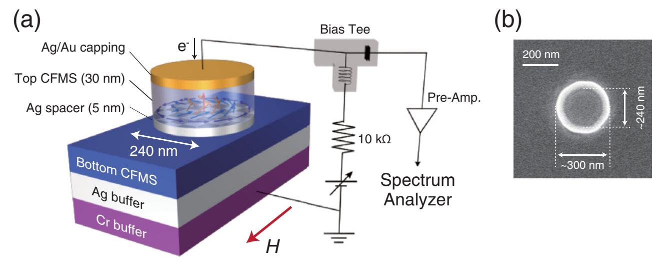

FIG. 1. (a) Schematic illustration of an STO with a CFMS vortex and a microwave measurement circuit. The 30-nm-thick top CFMS layer was patterned into a circular disk with a nominal diameter ($2r_0$) of 240 nm, whereas the 20-nm-thick bottom CFMS layer remained in an extended film. A positive dc current (I_{dc}) was defined as electrons flowing from the top CFMS layer to the bottom one. During the measurements, a static magnetic field (H) was applied along the in-plane direction, as denoted by an arrow. (b) Scanning electron microscopy image of the microfabricated nanopillar.

of the nanopillar had expanded from the designed value, and the edge was slightly distorted from an ideal circular shape. Meanwhile, the etching process is known to result in a tapered nanopillar (e.g., $2r_0 = 240$ nm for the top and $2r_0 = 300$ nm for the bottom of the nanopillar). For the following discussions, we will therefore use $2r_0 = 240$ nm for simplicity.

The microfabricated devices were connected to the rf circuit by using a two-terminal rf probe. To excite magnetization dynamics in the top CFMS layer, a dc current (I_{dc}) was fed into the devices by using a dc source meter through the dc port of a bias tee. Here, we use the convention that a positive I_{dc} corresponds to an electron flow from the top CFMS layer to the bottom one. The magnetization dynamics excited in the top CFMS layer was converted into a microwave signal via the GMR effect and was detected by a spectrum analyzer after being amplified by a preamplifier with a gain of +21 dB. The gain of the preamplifier was subtracted from the data presented here. All the measurements were performed at room temperature under the in-plane H applied along the easy axis of CFMS, i.e., the [110] direction of CFMS.

III. STRUCTURAL/MAGNETIC PROPERTIES OF CFMS THIN FILMS

Figures 2(a)–2(d) show RHEED patterns obtained from the Cr layer [(a) and (b)] and the top CFMS layer surface [(c) and (d)] for $x = 0.4$ with an electron beam incidence parallel to the MgO [100] [(a) and (c)] and MgO [110] directions [(b) and (d)]. These RHEED patterns revealed a flat surface and the epitaxial growth of the (001)-oriented Cr buffer and CFMS. Superlattice streaks were also clearly observed as denoted by the arrows in Fig. 2(c), indicating the chemical ordering of the CFMS layers into either $B2$ or $L2_1$ ordered structures. In addition to the RHEED patterns, in-plane XRD patterns obtained from 220 diffractions for each layer [Fig. 2(e)] revealed the epitaxial relationship of MgO [100] || Cr [110] || Ag [100] || CFMS [110]. The out-of-plane XRD patterns obtained from the prepared GMR stacking films with various x are shown in Fig. 3(a). In accordance with the RHEED patterns, the CFMS 200 superlattice diffractions as well as the CFMS 400 fundamental diffractions were clearly

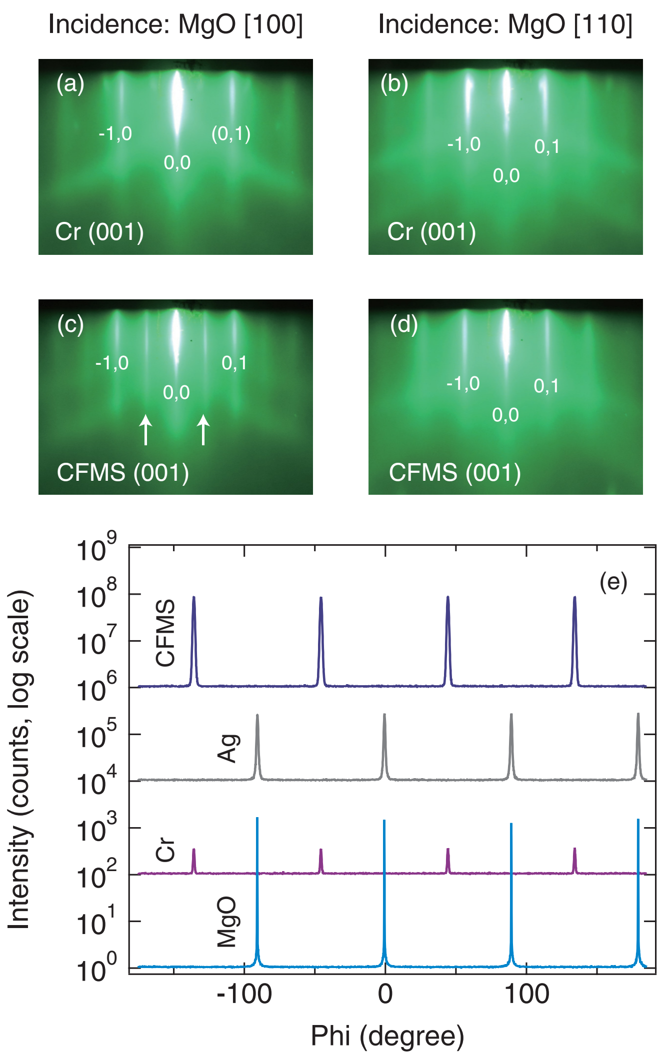

FIG. 2. RHEED patterns obtained from (a), (b) the Cr layer surface and (c), (d) the CFMS layer surface with the electron beam parallel to (a), (c) the MgO [100] and (b), (d) the MgO [110] directions. (e) In-plane XRD patterns obtained from the 220 diffractions of CFMS, Ag, Cr, and MgO.

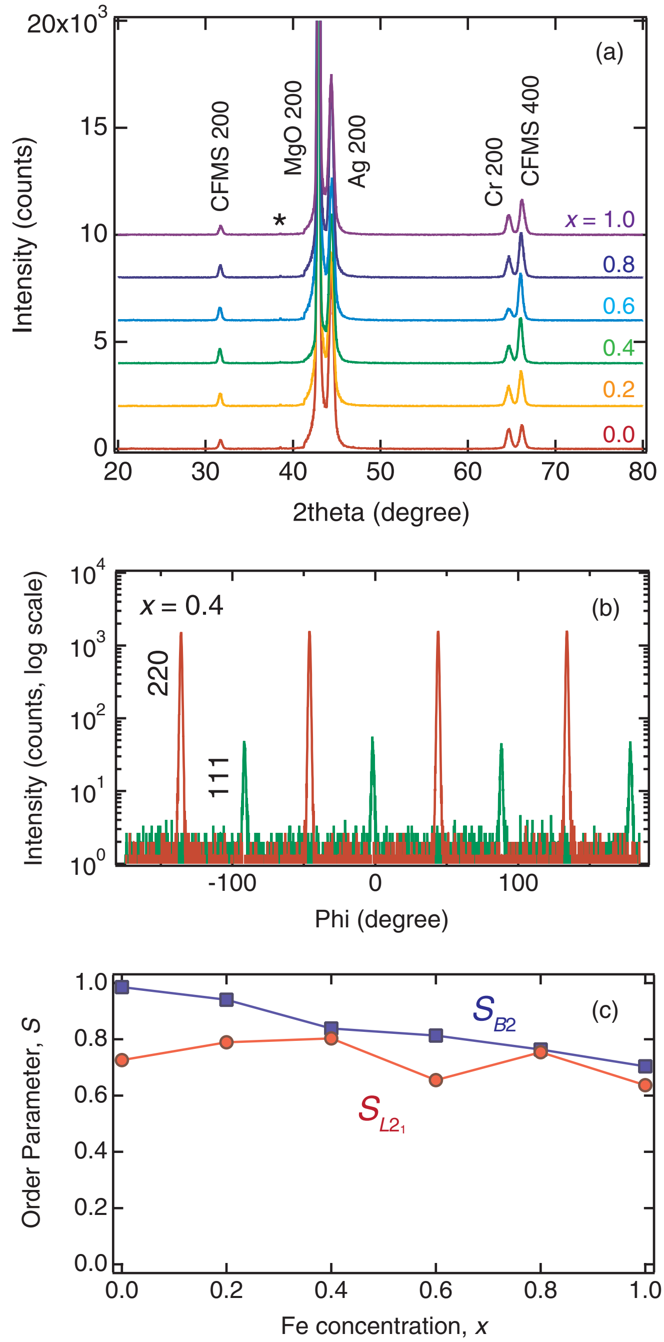

FIG. 3. (a) Out-of-plane XRD patterns obtained from CFMS films with various Fe concentrations (x). Peaks indicated by * correspond to the 200 diffractions of the MgO substrate from the Cu-Kβ source. (b) In-plane XRD patterns obtained from the CFMS film with $x = 0.4$. Red and green lines denote the CFMS 220 diffractions and the CFMS 111 diffractions, respectively. (c) Order parameters of the prepared CFMS films with various x. Blue and red symbols indicate the $B2$ order parameter (S_{B2}) and the $L2_1$ order parameter (S_{L2_1}), respectively.

observed for all the samples. Figure 3(b) displays the in-plane XRD patterns obtained from the CFMS film with $x = 0.4$. The appearance of the CFMS 220 fundamental diffraction and CFMS 111 superlattice diffraction having fourfold rotational symmetries with a phase difference of 45° around the CFMS [001] surface normal means $L2_1$ chemical ordering and the epitaxial growth of CFMS. S_{B2} and S_{L2_1} were estimated using Eqs. (1) and (2) and are plotted in Fig. 3(c) as a function of x. S_{B2} slightly decreased as x increased, whereas S_{L2_1} kept an almost constant value around 0.7 regardless of x. These high ordering parameters ensure the high spin polarization of prepared CFMS films [24,29,36].

Figures 4(a)–4(c) show the magnetization curves for the GMR stacking films with $x = 0.0$, 0.4, and 1.0, respectively, where the red (blue) curves correspond to magnetization curves measured with H applied along the CFMS [110] ([100]) direction. All the CFMS films exhibited small magnetocrystalline anisotropy with an easy axis along the CFMS [110] direction except for $x = 1.0$; the CFMS films with $x = 1.0$ had an easy axis along the CFMS [100] direction, but these changes in the magnitude and direction of the magnetocrystalline anisotropy would not affect the stability of vortices [37]. Figure 4(d) shows the dependencies of the

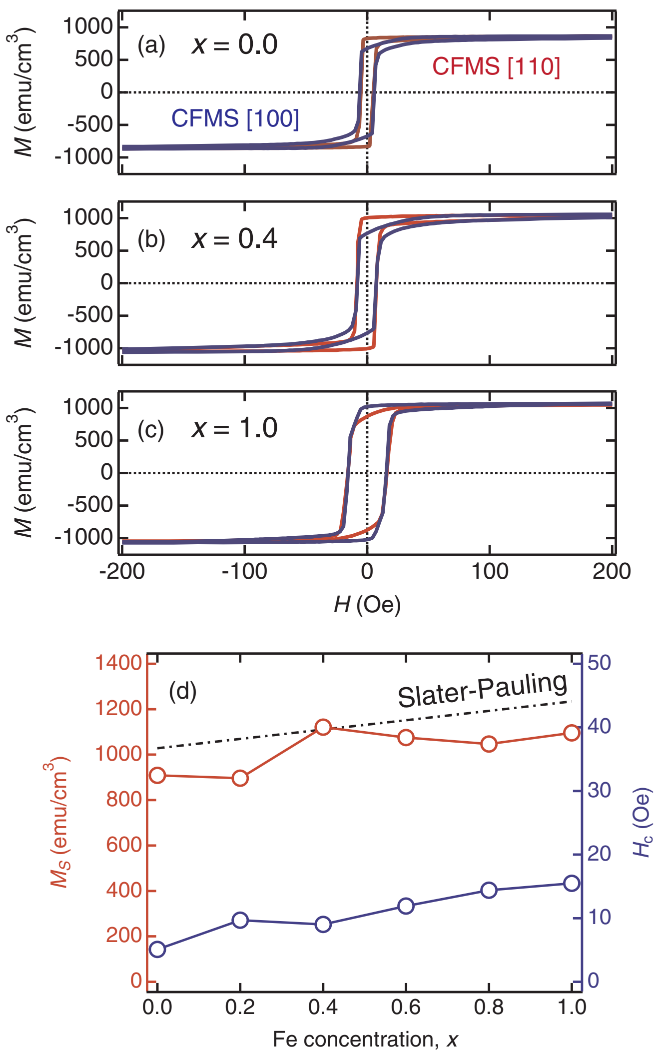

FIG. 4. (a)–(c) Magnetization curves obtained from the CFMS films with (a) $x = 0.0$, (b) $x = 0.4$, and (c) $x = 1.0$. Red (blue) lines correspond to magnetization curves for the fields applied along the CFMS [110] (CFMS [100]) direction. (d) x dependencies of M_s and H_c. The values of H_c were evaluated from easy-axis magnetization curves. The broken line represents the generalized Slater-Pauling behavior.

saturation magnetization (M_s) and the coercivity (H_c) on x. M_s gradually increased with Fe substitution in agreement with the generalized Slater-Pauling behavior (dotted line). H_c also showed almost monotonic increment against x with the minimum H_c of 5.1 Oe for $x = 0.0$ (CMS) and the maximum H_c of 15.5 Oe for $x = 1.0$ (CFS). It would be worth noting that the maximum value of H_c obtained for $x = 1.0$ was even smaller than that of the CFMS films prepared on a Cr buffer, which were used in our previous experiment for the direct observation of magnetic vortices in CFMS circular disks (23 Oe for the 30-nm-thick film) [37]. The reduction of H_c in the present CFMS films is attributed to the suppression of the atomic diffusion of Cr into the CFMS layers owing to the Ag layer insertion rather than the change in lattice matching since the difference in the lattice mismatch between Cr/CFMS (2.0%) and Ag/CFMS (2.2%) is only about 0.2% [24,36].

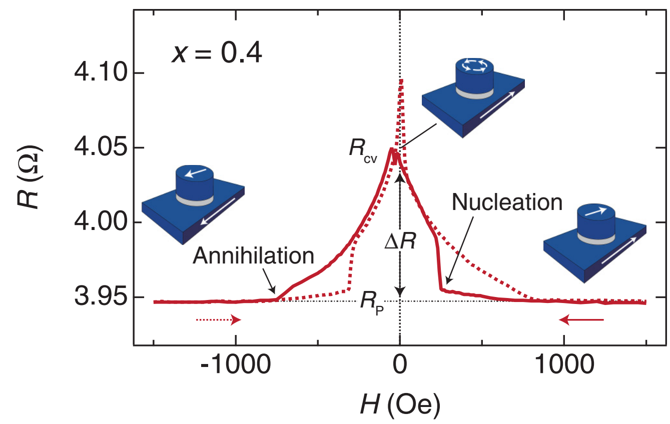

FIG. 5. Resistance-versus-field (R-H) curve measured by using a lock-in amplifier at $I_{dc} = 0$ mA for the device with $x = 0.4$. Possible magnetization configurations are schematically illustrated. R_P and R_{cv} correspond to the device resistances at the parallel state and at the centered-vortex state, respectively. ΔR is the difference between R_P and R_{cv}.

IV. SPIN-TORQUE-INDUCED VORTEX OSCILLATION IN MICROFABRICATED DEVICES

In this section, we describe the general oscillation properties of the microfabricated devices and then discuss the influences of the Fe substitution on the spin-torque oscillation. Figure 5 shows a resistance-versus-field (R-H) curve measured by using a lock-in amplifier at $I_{dc} = 0$ mA for the device with $x = 0.4$. Both the nucleation and the annihilation of a vortex in the top CFMS layer were clearly visible in this R-H curve around $H = \pm 250$ and ± 800 Oe, respectively. We also prepared a device with an ellipsoidal nanopillar with dimensions of 140 nm $\times$ 280 nm using the same film to check the resistance change from the parallel magnetization configuration to the antiparallel one. The R-H curve revealed that the resistance change was 0.29 Ω, which is about twice as large as that observed in Fig. 5 near $H = 0$ Oe. Therefore, the peak in R observed around $H = 0$ Oe may have originated from the transient magnetization process undergoing the 90° magnetization configuration rather than the antiparallel one.

Figure 6 shows differential resistance (dV/dI) as a function of I_{dc} and power spectral density (PSD) spectra measured while changing I_{dc} at $H = 300$ Oe. It can be seen that the dV/dI curve was almost reversible for this I_{dc} range; i.e., there was no hysteresis associated with the STT-induced magnetization switching. One can see a small peak in the dV/dI curve around $I_{dc} = 2$ mA, and correspondingly, a single peak appears in each rf spectrum for $I_{dc} \geqslant 2.4$ mA, indicating the onset of spin-torque oscillation at an onset current (I_{onset}) of 2.4 mA. This I_{onset} corresponds to a current density of 5.3×10^{10} A/m^2, which is about 5 times smaller than that required to excite vortex-like magnetization dynamics in a point-contact-based STO using CFMS with a nominal contact diameter of 140 nm [33]. The small I_{onset} and absence of hysteresis in the dV/dI curve suggest that the microwave signal resulted from the excitation of dynamics in a *naturally* formed magnetic vortex rather than a current-induced one [33,39].

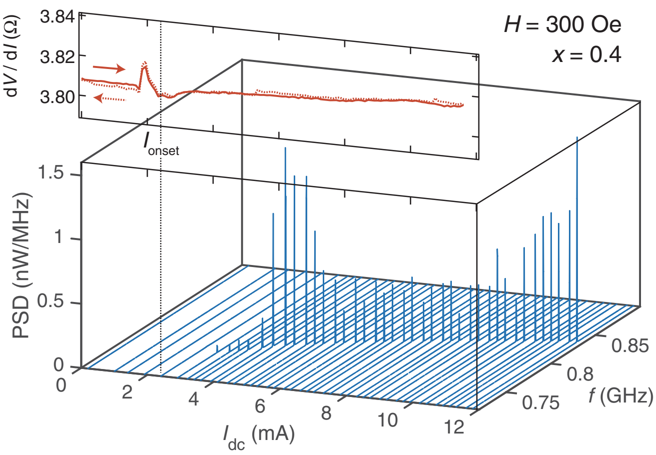

FIG. 6. Differential resistance (dV/dI) curve and corresponding power spectral density (PSD) spectra measured at $H = 300$ Oe. Black dashed line indicates the dc current (I_{dc}) value at which a peak appears in the PSD spectrum (I_{onset}). The Fe concentration of CFMS was $x = 0.4$.

Figures 7(a)–7(d) show the I_{dc} dependencies of f_0, Δf, P_{out}, and the inverse power $1/P_{out}$ obtained from PSD spectra measured at $H = 250$ Oe for the device with $x = 0.4$. At $I_{onset} = 2.4$ mA, an oscillation peak appeared around $f_0 = 0.8$ GHz similar to that observed in Fig. 6, and Δf rapidly decreased down to below 1 MHz as I_{dc} increased from I_{onset}. This behavior is characteristic of the transition from thermally excited magnetization dynamics to the stable (self-sustained) oscillation of an STO [40]. In order to determine I_{th}, we plotted $1/P_{out}$ against I_{dc}, and I_{th} was estimated from the I_{dc} intercept

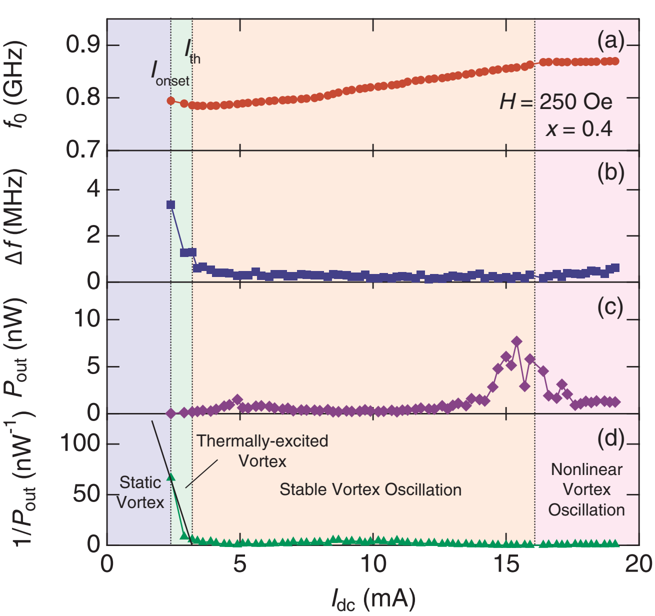

FIG. 7. I_{dc} dependencies of oscillation parameters. (a) Oscillation frequency f_0, (b) oscillation linewidth Δf, (c) output power P_{out}, and (d) inverse power $1/P_{out}$. Black line in (d) is a linear fit to the experimental data. These parameters were obtained from PSD spectra measured for the device with $x = 0.4$ at $H = 250$ Oe.

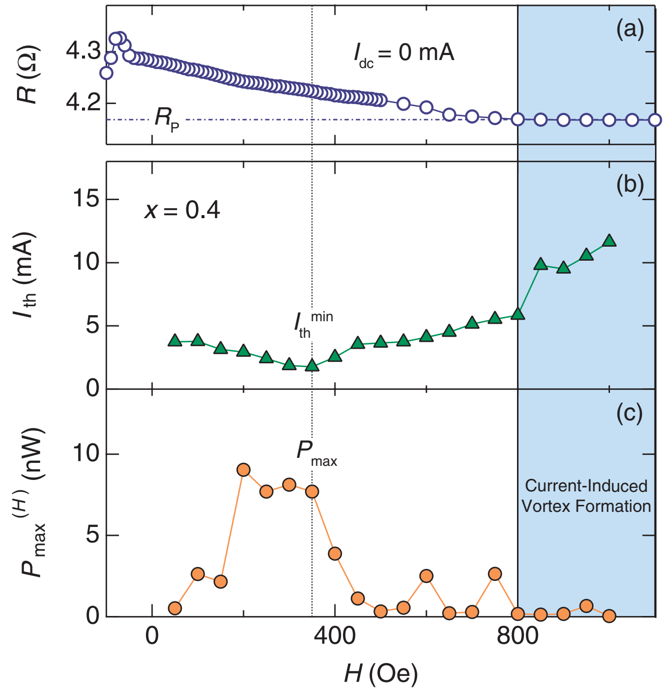

FIG. 8. (a) R-H curve measured for a device with $x = 0.4$ at $I_{dc} = 0$ mA. (b), (c) H dependencies of (b) threshold current I_{th}, and (c) maximum output power $P_{max}^{(H)}$.

in a low-I_{dc} region [40]. In the stable vortex oscillation region, f_0 almost linearly increased as I_{dc} increased as expected from the *linear* tunability of a vortex STO driven by the Oersted field. Well above I_{th}, Δf became almost constant around 150 kHz, and P_{out} reached a maximum value of $P_{max}^{250\text{ Oe}} = 7.7$ nW at $I_{dc} = 15.4$ mA. For $I_{dc} > 16$ mA, however, f_0 became almost constant, and a slight increase of Δf was observed. In addition to this increase of Δf, we also observed asymmetric distortion of the spectral shape in this current region (not shown), which resembles the spectral distortion in an STO near the threshold [41]. We therefore attribute the change of the oscillation characteristics for $I_{dc} > 16$ mA to the nonlinear oscillation of the present device. Details on the mechanism of the oscillation in the nonlinear region are beyond the scope of this study, but the oscillation features would originate from strong distortion of the vortex core trajectory caused by an increased STT and the edge roughness of the nanopillar.

To quantitatively characterize the oscillation parameters for each device with different x, I_{th} and the (field-dependent) maximum output power ($P_{max}^{(H)}$) were determined by changing H. Figures 8(b) and 8(c) are the H dependencies of I_{th} and $P_{max}^{(H)}$ along with the corresponding R-H curve measured at $I_{dc} = 0$ mA [Fig. 8(a)]. I_{th} decreased with the application of a small magnetic field H and showed a minimum around $H = 300$ Oe. Correspondingly, a peak appeared in $P_{max}^{(H)}$ around this H region. To maximize the radius of the gyrotropic motion of a vortex core (or to minimize I_{th}), a parabolic potential in which the local minimum is located at the center of the disk is required. On the other hand, the dipolar magnetic field coming from the bottom CFMS layer modifies the energy landscape, and that would lead to the reduction of P_{out} as well

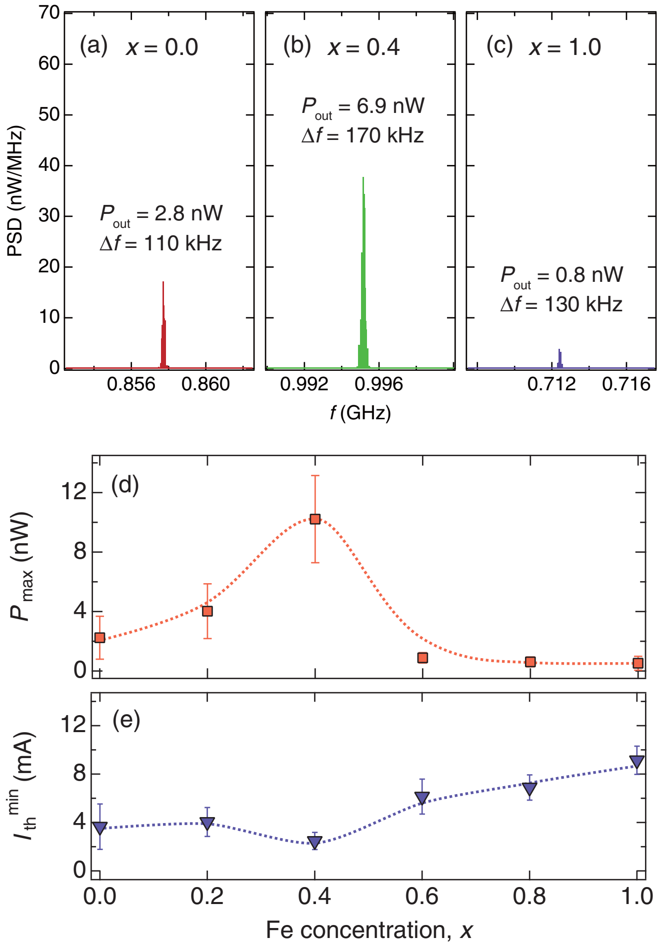

FIG. 9. (a)–(c) PSD spectra obtained from various x. (d), (e) x dependencies of (d) maximum output power available for a device P_{out}, and (e) minimum threshold current $I_{\mathrm{th}}^{\mathrm{min}}$.

as the increase of I_{th}. The maximum power available for an STO (P_{max}) was therefore defined as $P_{\mathrm{max}}^{(H)}$ at which I_{th} was minimized ($I_{\mathrm{th}} = I_{\mathrm{th}}^{\mathrm{min}}$). For $H > 800$ Oe, as can be seen in the R-H curve, although a magnetic vortex was annihilated from the top CFMS layer when $I_{\mathrm{dc}} = 0$ mA, the Oersted field originating from the I_{dc} injection increased the stability of the vortex state. This current-induced vortex formation is identified by the significant increase in I_{th}.

Figures 9(a)–9(c) are the representative PSD spectra obtained from (a) $x = 0.0$ (CMS), (b) $x = 0.4$, and (c) $x = 1.0$ (CFS). Although there were slight differences in the conditions for the oscillations, coherent oscillations with Δf below 200 kHz and a very high quality factor $f_0/\Delta f > 5000$ were achieved regardless of x. Another signature of the present vortex oscillator is the large P_{out} despite the reduced magnetoresistance caused by the topological spin relaxation associated with the in-plane electron flow through the vortex layer [42]. For $x = 0.0$ (CMS), P_{out} is about three times larger even compared with the CMS-based nonvortex STO under the same measurement configuration [31]. Moreover, P_{out} was clearly enhanced by the moderate Fe substitution. Unfortunately, we found it was difficult to quantitatively characterize a change in Δf associated with Fe substitution only from the frequency-domain measurement. Direct analysis of the oscillation noises [43–45] would provide a better insight into the effect of Fe substitution on the spectral purity of CFMS-based STOs. Instead, we here focus on P_{max} and I_{th} as determined in Fig. 8.

The dependencies of P_{max} and I_{th} on x are plotted in Figs. 9(d) and 9(e), respectively. The values of P_{out} and I_{th} were taken over four devices for each x, and the average values are plotted with error bars representing the standard deviation. P_{out} was increased as x increased from 0.0 (CMS), and it reached a maximum of 10.2 nW at $x = 0.4$. A further increase of x lead to a sharp drop in P_{out}, and P_{out} became almost constant for $0.6 \leqslant x \leqslant 1.0$. In comparison, an almost linear change was observed for the dependence of I_{th} on x, as shown in Fig. 9(e). Since the energy required to displace a vortex core is to be proportional to M_{s} and H_{c}, I_{th} should reflect the linear dependencies of M_{s} and H_{c} observed in un-patterned films [Fig. 4(d)]. More importantly, in addition to the linear trend of I_{th}, there can be seen a remarkable reduction of I_{th} around $x = 0.4$. The reduction of I_{th} is attributed to the increased spin polarization of CFMS as observed in the x dependence of P_{out}. Thus, the experimental results displayed in Figs. 9(d) and 9(e) clearly show that the enhancement of the output power and the reduction of the threshold current were achieved simultaneously. This fact is in agreement with a model for spin-torque oscillation, in which P_{out} (I_{th}) is (inversely) proportional to the spin polarization of ferromagnetic layers. This also indicates the importance of developing highly spin-polarized ferromagnetic materials from the points of view of realizing both a high P_{out} and low I_{th} in a vortex STO.

V. DISCUSSION

According to a classical theory, the gyrotropic motion of a vortex core in an STO can be described by Thiele's equation [46,47]:

$$\boldsymbol{G} \times \frac{d\boldsymbol{X}}{dt} + \frac{\partial W}{\partial \boldsymbol{X}} = 0, \tag{3}$$

where $\boldsymbol{X} = x\boldsymbol{e}_x + y\boldsymbol{e}_y$ is the two-dimensional position vector of the vortex core, $W(\boldsymbol{X})$ is the potential energy of the shifted vortex, and the gyrovector ($\boldsymbol{G}$) is perpendicular to the device plane ($\boldsymbol{G} = G\boldsymbol{e}_z$) with the magnitude $G = (2\pi L M_{\mathrm{s}}/\gamma)p$ (γ: modulus of the gyromagnetic ratio, $p = \pm 1$: polarization of the vortex core). When $|\boldsymbol{X}| = r$ is small, the variation of the potential energy can be expressed as [48]

$$W(\boldsymbol{X}) = W(0) + \frac{1}{2}\kappa|\boldsymbol{X}|^2 + O\left(\frac{|\boldsymbol{X}|}{r_0}\right)^4. \tag{4}$$

The vortex core stiffness (κ) is given by the sum of stiffness arising from the magnetostatic energy and the Zeeman energy due to the Oersted field as follows [48]:

$$\kappa(I_{\mathrm{dc}}) = \kappa_{\mathrm{ms}} + \kappa_{\mathrm{Oe}} \times \frac{I_{\mathrm{dc}}}{\pi r_0^2}, \tag{5}$$

where $\kappa_{\mathrm{ms}} = \frac{10}{9}\mu_0 M_{\mathrm{s}}^2 L^2/r_0$ and $\kappa_{\mathrm{Oe}} = 0.85 C \mu_0 M_{\mathrm{s}} r_0 L$. $C = +1\,(-1)$ is the chirality of the vortex core parallel (antiparallel) to the Oersted field formed by $I_{\mathrm{dc}} > 0$. Then, the frequency of

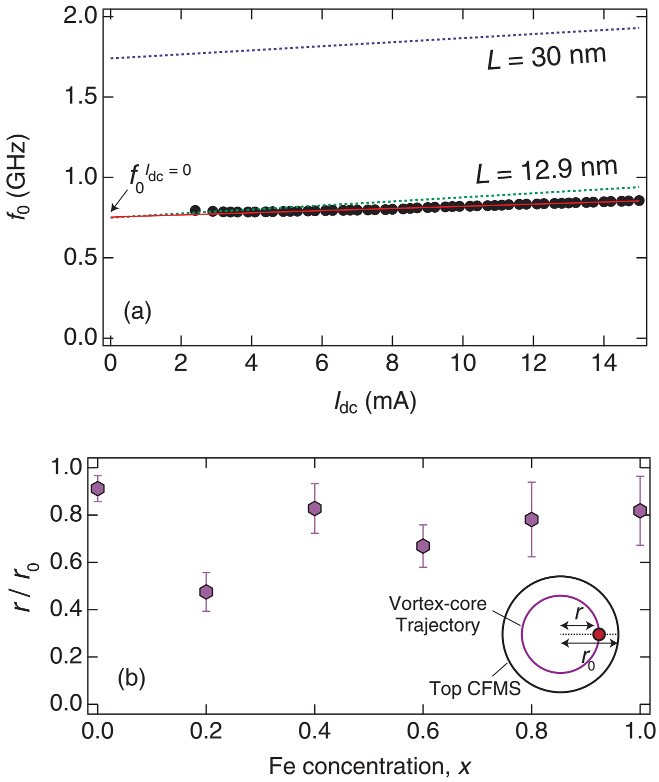

FIG. 10. (a) f_0 as a function of I_{dc}. Red line is a linear fit to the experimental data (black symbols). Blue and green dotted lines represent data calculated using Eq. (6) with $L = 30$ nm and $L = 12.9$ nm, respectively. (b) x dependence of normalized vortex core trajectory (r/r_0) at which P_{out} is maximized.

the gyrotropic mode [$f_0^{calc}(I_{dc})$] is expressed as

$$f_0^{calc}(I_{dc}) = \frac{\kappa(I_{dc})/G}{2\pi} = \frac{\left(\kappa_{ms} + \kappa_{Oe} I_{dc}/\pi r_0^2\right)/G}{2\pi}. \tag{6}$$

This gives a zero-current oscillation frequency $f_0^{I_{dc}=0}$ of 1.74 GHz and a slope df/dI_{dc} of 1.26×10^{-2} GHz/mA, which are plotted by the blue dotted line in Fig. 10(a). Although the analytical result seems to well reproduce the slope of the experimental result (black symbols) without any fitting parameter, the experimentally obtained $f_0^{I_{dc}=0}$ was found to be about half of the calculated one. Accordingly, the *effective* thickness estimated from the actual $f_0^{I_{dc}=0}$ was found to be $L = 12.9$ nm. These deviations between the experiment and the analytical prediction would be caused by the existence of the nontrivial mass of a vortex [49], but in the case of a vortex-based STO, it would be rather important to take into account a nonuniformity in the vortex core motion along the thickness direction as demonstrated in the early work using an STO with thick vortex layer [14]. Since the spin-diffusion length of a Co-based Heusler alloy is typically of the order of a few nanometers [27], which is the same order as Permalloy (Fe-Ni alloy) [50], the spin accumulation in the Heusler alloy layer mostly dissipated in the interface region with the spacer layer. Therefore, the STT was only effective for the magnetic moments close to the Ag/CFMS interface.

As discussed above, there would be a significant inhomogeneity in the vortex core motion along the thickness direction, yet it is possible to estimate the radius of the vortex core trajectory near the Ag spacer/top CFMS interface; as the time-varying resistance of a vortex STO is given by

$$R(t) = R_{cv} + \left(\Delta R \times \frac{r}{r_0}\right) \sin(2\pi f_0 t), \tag{7}$$

the output power of a vortex STO can be expressed as [45]

$$P_{out} = \frac{I_{dc}^2}{2} \frac{R_L}{(R_{cv} + R_L)^2} \times \left(\Delta R \times \frac{r}{r_0}\right)^2, \tag{8}$$

where $R_L = 50\ \Omega$ is the load resistance. The estimated normalized radius of the vortex core trajectory (r/r_0) at which P_{out} is maximized is plotted as a function of x in Fig. 10(b). The gyration radii were found to be about 75% of the top CFMS layer radii for most x, which are larger than the one reported for a vortex MTJ-STO (50% of the disk radius) [45]. The remarkable error for $x = 0.4$ shown in Fig. 9(d) can be explained by Eq. (8); P_{out} became more sensitive against the change of r/r_0 as the magnetoresistance ΔR increased; i.e., at a given variation of r/r_0, the variation of P_{out} should be larger for the devices showing a larger ΔR. Importantly, for the present devices, the large gyration radii were achieved without significant linewidth broadening, which may have resulted from the improved stability of magnetic vortices owing to the thick CFMS layer and the Oersted field formed by the relatively large I_{dc} injection [although there was slight linewidth broadening due to the distortion of the vortex core trajectory as observed in Fig. 7(b), which may have partly originated from the edge roughness of the nanopillars]. Therefore, this experimental result indicates that the CFMS-based GMR junction is advantageous in realizing stable and large-amplitude vortex oscillations. Further improvements of P_{out} and $f_0/\Delta f$ can be expected by optimizing the top CFMS layer thickness and/or utilizing two-coupled vortex dynamics [15,20].

VI. CONCLUSION

We investigated STT-driven vortex oscillation in CFMS circular disks with various Fe-Mn compositions. Owing to the small magnetocrystalline anisotropy and small coercivity of CFMS, the microfabricated devices exhibited clear vortex oscillations regardless of x. P_{max} was remarkably enhanced by the Fe substitution, and a maximum output power P_{max} of 10.2 nW was achieved for $x = 0.4$. At the same time, I_{th} was minimized at $x = 0.4$, which was in agreement with a model for spin-torque oscillation. By comparing to an analytical theory, the vortex dynamics excited in the present devices were found to be inhomogeneous along the thickness direction. Nevertheless, the radii of the vortex core trajectory at the Ag spacer/top CFMS interface were estimated to be ~75% of the top CFMS radii. Since these large gyration radii were achieved without significant linewidth broadening, the CFMS-based vortex GMR-STO would be useful for investigating the large-amplitude gyration motion of a vortex core. The present experimental results also indicate the potential of highly spin-polarized Heusler alloys in the development of vortex-based GMR-STOs compatible with practical microwave applications.

ACKNOWLEDGMENTS

The authors acknowledge S. Tsunegi, H. Kubota (Japan National Institute of Advanced Industrial Science and Technology), and T. Chiba (IMR, Tohoku University) for their fruitful discussions. This work was supported by the Division for Interdisciplinary Advanced Research and Education, Tohoku University, and a Japan Society for the Promotion of Science Research Fellowship for Young Scientists. The device fabrication was partially performed at the Cooperative Research and Development Center for Advanced Materials, IMR, Tohoku University.

[1] L. Berger, Phys. Rev. B **54**, 9353 (1996).
[2] J. C. Slonczewski, J. Magn. Magn. Lett. **159**, L1 (1996).
[3] E. B. Myers, D. C. Ralph, J. A. Katine, R. N. Luie, and R. A. Burman, Science **285**, 867 (1999).
[4] J. A. Katine, F. J. Albert, R. A. Buhrman, E. B. Myers, and D. C. Ralph, Phys. Rev. Lett. **84**, 3149 (2000).
[5] Z. Diao, D. Apalkov, M. Pakala, Y. Ding, A. Panchula, and Y. Huai, Appl. Phys. Lett. **87**, 232502 (2005).
[6] M. Tsoi, A. G. M. Jansen, J. Bass, W. C. Chiang, V. Tsoi, and P. Wyder, Nature (London) **406**, 46 (2000).
[7] S. I. Kiselev, J. C. Sankey, I. N. Krivorotov, N. C. Emeley, R. J. Schoelkopf, R. A. Burman, and D. C. Ralph, Nature (London) **425**, 380 (2003).
[8] Y. Ji, C. L. Chien, and M. D. Stiles, Phys. Rev. Lett. **90**, 106601 (2003).
[9] V. E. Demidov, S. Urazhdin, H. Ulrichs, V. Tiberkevich, A. Slavin, D. Baither, G. Schmitz, and S. O. Demokritov, Nat. Mater. **11**, 1028 (2012).
[10] W. H. Rippard, M. R. Pufall, S. Kaka, S. E. Russek, and T. J. Silva, Phys. Rev. Lett. **92**, 027201 (2004).
[11] A. V. Nazarov, H. M. Olson, H. Cho, K. Nikolaev, Z. Gao, S. Stokes, and B. B. Pant, Appl. Phys. Lett. **88**, 162504 (2006).
[12] A. M. Deac, A. Fukushima, H. Kubota, H. Maehara, Y. Suzuki, S. Yuasa, Y. Nagamine, K. Tsunekawa, D. D. Djayaprawira, and N. Watanabe, Nat. Phys. **4**, 803 (2008).
[13] R. H. Liu, W. L. Lim, and S. Urazhdin, Phys. Rev. Lett. **110**, 147601 (2013).
[14] V. S. Pribiag, I. N. Krivotov, G. D. Fuchs, P. M. Braganca, O. Ozatay, J. C. Sankey, D. C. Ralph, and R. A. Buhrman, Nat. Phys. **3**, 498 (2007).
[15] N. Locatelli, V. V. Naletov, J. Grollier, G. de Loubens, V. Cros, C. Deranlot, C. Ulysse, G. Faini, O. Klein, and A. Fert, Appl. Phys. Lett. **98**, 062501 (2011).
[16] F. Sanches, V. Tiberkevich, K. Y. Guslienko, J. Sinha, M. Hayashi, O. Prokopenko, and A. N. Slavin, Phys. Rev. B **89**, 140410(R) (2014).
[17] A. Ruotolo, V. Cros, B. Georges, A. Dussaux, J. Grollier, C. Deranlot, R. Guillemet, K. Bouzehouane, S. Fusil, and A. Fert, Nat. Nanotechnol. **4**, 528 (2009).
[18] S.-P. Watelot, J.-V. Kim, A. Ruotolo, R. M. Otxoa, K. K. Bouzehouane, J. Grollier, A. Vansteenkiste, B. V. Wiele, V. Cros, and T. Devolder, Nat. Phys. **8**, 682 (2012).
[19] A. Dussaux, B. Georges, J. Grollier, V. Cros, A. V. Khvalkovskiy, A. Fukushima, M. Konoto, H. Kubota, K. Yakushiji, S. Yuasa, K. A. Zvezdin, K. Ando, and A. Fert, Nat. Commun. **1**, 8 (2010).
[20] S. Tsunegi, H. Kubota, K. Yakushiji, M. Konoto, S. Tamaru, A. Fukushima, H. Arai, H. Imamura, E. Grimaldi, R. Lebrun, J. Grollier, V. Cros, and S. Yuasa, Appl. Phys. Express **7**, 063009 (2014).
[21] A. Hamadeh, N. Locatelli, V. V. Naletov, R. Lebrun, G. de Loubens, J. Grollier, O. Klein, and V. Cros, Phys. Rev. Lett. **112**, 257201 (2014).
[22] T. Ishikawa, T. Marukame, H. Kijima, K.-I. Matsuda, T. Uemura, M. Arita, and M. Yamamoto, Appl. Phys. Lett. **89**, 192505 (2006).
[23] S. Tsunegi, Y. Sakuraba, M. Oogane, K. Takanashi, and Y. Ando, Appl. Phys. Lett. **93**, 112506 (2008).
[24] Y. Sakuraba, T. Iwase, K. Saito, S. Mitani, and K. Takanashi, Appl. Phys. Lett. **94**, 012511 (2009).
[25] N. Tezuka, N. Ikeda, A. Miyazaki, S. Sugimoto, M. Kikuchi, and K. Inomata, Appl. Phys. Lett. **89**, 112514 (2006).
[26] R. Shan, H. Sukegawa, W. H. Wang, M. Kodzuka, T. Furubayashi, T. Ohkubo, S. Mitani, K. Inomata, and K. Hono, Phys. Rev. Lett. **102**, 246601 (2009).
[27] T. M. Nakatani, T. Furubayashi, S. Kasai, H. Sukegawa, Y. K. Takahashi, S. Mitani, and K. Hono, Appl. Phys. Lett. **96**, 212501 (2010).
[28] Y. K. Takahashi, A. Srinivasan, B. Varaprasad, A. Rajanikanth, N. Hase, T. M. Nakatani, S. Kasai, T. Furubayashi, and K. Hono, Appl. Phys. Lett. **98**, 152501 (2011).
[29] Y. Sakuraba, M. Ueda, Y. Miura, K. Sato, S. Bosu, K. Saito, M. Shirai, T. J. Konno, and K. Takanashi, Appl. Phys. Lett. **101**, 252408 (2012).
[30] Z. Wen, T. Kubota, T. Yamamoto, and K. Takanashi, Sci. Rep. **5**, 18387 (2015).
[31] R. Okura, Y. Sakuraba, T. Seki, K. Izumi, M. Mizuguchi, and K. Takanashi, Appl. Phys. Lett. **99**, 052510 (2011).
[32] T. Seki, Y. Sakuraba, H. Arai, M. Ueda, R. Okura, H. Imamura, and K. Takanashi, Appl. Phys. Lett. **105**, 092406 (2014).
[33] T. Yamamoto, T. Seki, T. Kubota, H. Yako, and K. Takanashi, Appl. Phys. Lett. **106**, 092406 (2015).
[34] T. Kubota, S. Tsunegi, M. Oogane, S. Mizukami, T. Miyazaki, H. Naganuma, and Y. Ando, Appl. Phys. Lett. **94**, 122504 (2009).
[35] L. J. Singh, Z. H. Barber, Y. Miyoshi, Y. Bugoslavsky, W. R. Branford, and L. F. Cohen, Appl. Phys. Lett. **84**, 2367 (2004).
[36] Y. Sakuraba, K. Izumi, T. Iwase, S. Bosu, K. Saito, K. Takanashi, Y. Miura, K. Futatsukawa, K. Abe, and M. Shirai, Phys. Rev. B **82**, 094444 (2010).
[37] T. Yamamoto, T. Seki, M. Kotsugi, and K. Takanashi, Appl. Phys. Lett. **108**, 152402 (2016).
[38] Y. Takamura, R. Nakane, and S. Sugahara, J. Appl. Phys. **105**, 07B109 (2009).

[39] T. Devolder, J.-V. Kim, P. Crozat, C. Chappert, M. Manfrini, M. van Kampen, W. V. Roy, L. Lagae, G. Hrkac, and T. Schrefl, Appl. Phys. Lett. **95**, 012507 (2009).
[40] A. Slavin and V. Tiberkevich, IEEE Trans. Magn. **45**, 1875 (2009).
[41] J.-V. Kim, Q. Mistral, C. Chappert, V. S. Tiberkevich, and A. N. Slavin, Phys. Rev. Lett. **100**, 167201 (2008).
[42] S. Urazhdin, C. L. Chien, K. Y. Guslienko, and L. Novozhilova, Phys. Rev. B **73**, 054416 (2006).
[43] M. W. Keller, M. R. Pufall, W. H. Rippard, and T. J. Silva, Phys. Rev. B **82**, 054416 (2010).
[44] M. Quinsat, D. Gusakova, J. F. Sierra, J. P. Michel, D. Houssameddine, B. Delaet, M. C. Cyrille, U. Ebels, B. Dieny, L. D. Buda-Prejbeanu, J. A. Katine, D. Mauri, A. Zeltser, M. Prigent, J. C. Nallatamby, and R. Sommet, Appl. Phys. Lett. **97**, 182507 (2010).
[45] E. Grimaldi, A. Dussaux, P. Bortolotti, J. Grollier, G. Pillet, A. Fukushima, H. Kubota, K. Yakushiji, S. Yuasa, and V. Cros, Phys. Rev. B **89**, 104404 (2014).
[46] A. A. Thiele, Phys. Rev. Lett. **30**, 230 (1972).
[47] K. Y. Guslienko, B. A. Ivanov, V. Novosad, Y. Otani, H. Shima, and K. Fukamichi, J. Appl. Phys. **91**, 8037 (2002).
[48] A. Dussaux, A. V. Khvalkovskiy, P. Bortolotti, J. Grollier, V. Cros, and A. Fert, Phys. Rev. B **86**, 014402 (2012).
[49] K. Y. Guslienko, G. N. Kakazei, J. Ding, X. M. Liu, and A. O. Adeyeye, Sci. Rep. **5**, 13881 (2015).
[50] T. Kimura, J. Hamrle, and Y. Otani, Phys. Rev. B **72**, 014461 (2005).